Supporting Information

Hansen and Dragoi 10.1073/pnas.1102017108

SI Methods

Local Field Potentials (LFPs). Our LFP data were sampled at 1,000 Hz and filtered between 0.5 Hz and 100 Hz using a fourth-order Butterworth filter. We designed the filter to have less than three peak-to-peak ripples in the passband and at least 50-dB attenuation in the stopband. Given the specific properties of this filter and the potential dampening of high gamma, we also analyzed the data using a fourth-order Butterworth filter with a cutoff frequency of 200 Hz. Both methods yielded highly similar results. To remove line artifacts, we applied a digital notch at 60 Hz (fourth-order elliptic filter, 0.1-dB peak-to-peak ripples, 40-dB stopband attenuation; the cross-correlation between the monitor 60-Hz refresh pulses and spikes and LFPs for our entire population failed to find a signature of locking). All filtering was applied by using forward and backward filtering to obtain zero phase shifts. To correct for the time delays induced in the LFP signals by the filters in headstages and preamplification boards we used the software correction FPAlign provided by Plexon (http://www.plexon.com/downloads.html). We discarded all LFPs that had more than three points outside the mean ± 4 SD to avoid influence of irregular artifact noise from muscle activity or other sources. We assessed whether LFPs are selective for orientation and whether adaptation affects LFP amplitude tuning by performing a trial-by-trial ANOVA.

Current-Source Density. For each recording session, we verified the laminar position of the electrode contacts by computing the evoked response potential (ERP) profile for brief visual stimulation during a passive fixation task. Briefly, monkeys were exposed to a full-field black screen that flashed white for 100 ms and then returned to black. The local field potential (LFP) time-series was recorded using 16-channel laminar probes. Fluctuation changes in LFP amplitude, in response to the white flash, were processed to obtain ERP traces for each contact (ERPs were recorded for 100 trials) (1, 2). We computed the current-source density (CSD) according to the second spatial derivative of the LFP time-series across laminar contacts (100-μm spacing) using the iCSD toolbox for MATLAB (http://software.incf.org/software/csdplotter/home) (3, 4). This analysis allowed us to accurately identify the polarity inversion accompanied by the sink-source configuration at the base of layer 4 (the sink is inside layer 4). Using homemade MATLAB programs we analyzed the laminar CSD profile to verify the presence of a primary sink in the granular layer in each of the 20 recording sessions. This was accomplished by locating the sink-driven negative polarity in the CSD plot and then computing the center of mass of the granular sink. We obtained a single coordinate from this analysis, consisting of the contact number and the time (in ms) when the sink was largest (center of mass). The contact with the largest sink center of mass served as the granular layer reference at 0 μm. We then analyzed all of the contacts above and below the reference and grouped them (according to their sink/source waveform characteristics; Fig. S2) into one of three possible layers: supragranular, granular, and infragranular.

In addition, several controls were performed to validate our method for identifying cortical layers: (*i*) we observed that micrometer advancement of the laminar electrode was highly correlated with a corresponding shift in the center of mass of the granular sink ($r = 0.89$, $P = 0.0001$, Pearson correlation); (*ii*) shuffling electrode contacts as a function of cortical depth destroyed the laminar-specific CSD profile; and (*iii*) vertical penetrations across cortical layers revealed a highly consistent columnar organization based on the orientation preference of the LFPs (Fig. S3).

Neuronal Discrimination. As a measure of neuronal discrimination performance, we calculated the neurons' capacity (d') to discriminate between orientations within 22.5° of the cell's preferred orientation as the difference between the mean spike rates ($\mu_{\theta\pm22.5}$ and μ_θ) at the two nearby orientations divided by the root mean square SD ($\sigma_{\theta\pm22.5}$ and σ_θ) (5, 6).

$$d' = \frac{(\mu_{\theta\pm22.5} - \mu_\theta)}{\sqrt{\frac{\sigma^2_{\theta\pm22.5} + \sigma^2_\theta}{2}}}. \quad [1]$$

These measures, mean firing rate and response SD, were calculated from the trial-by-trial mean responses during the entire 300-ms presentation of the test stimulus in each condition (control and adaptation). Mean d' was calculated by averaging the d' values obtained for each test orientation pair around the preferred orientation, θ (i.e., θ ± 22.5°).

Coefficient of Variation (CV). As a measure of neuronal precision, we calculated the variation in the neurons' interspike interval (ISI) between test orientations within 22.5° of the cell's preferred orientation. CV was computed as follows:

$$\frac{\sigma_{ISI}}{\overline{ISI}}. \quad [2]$$

These measures, SD of the ISI and mean ISI, were calculated from the trial-by-trial responses during the entire 300-ms presentation of the test stimulus in each condition (control and adaptation). Mean CV was calculated by averaging the CV values obtained for each test orientation pair around the preferred orientation, θ (i.e., θ ± 22.5°) (Fig. S8).

Spike-Field Coherence (SFC). We used multitaper spectral analysis to compute SFC, which measures the degree of synchronization between neurons and LFPs as a function of frequency. In general, the coherence between two signals (x and y) recorded at different sites is a complex quantity whose magnitude is a measure of the phase synchrony for frequency f.

Coherence is an absolute value that varies between 0 and 1 (e.g., a value of 1 indicates a perfect phase relationship between the firing of the spikes to the fluctuations of the LFP). Coherence is defined as:

$$C_{yx}(f) = \frac{S_{yx}(f)}{\sqrt{S_x(f)S_y(f)}}, \quad [3]$$

where $S_x(f)$ and $S_y(f)$ represent the auto-spectra and $S_{yx}(f)$ the cross-spectrum of the two signals x and y. Auto-spectra and cross-spectra are averaged across trials before the coherency calculation (7, 8). In an attempt to eliminate any bias from differing sample sizes, the same number of trials for each condition (adaptation and control) was used for the calculation of coherence for a given pair. Importantly, the length of data included in each condition was also constant.

Specifically, we used the Chronux function *coherencycpt*, which computes the multitaper SFC for a continuous signal (LFP) and point process data (spike-train) according to an optimal family of

orthogonal tapers derived from Slepian functions (7–10). The number of tapers was calculated according to the formula:

$$K = 2^{*}TW - 1, \quad [4]$$

where K is the highest number of tapers that can be used while preserving optimal time-frequency concentration of the data windowing available from the Slepian taper sequences, T is the length of the data in seconds, and W is the half-bandwidth of the multitaper filter. For our analysis we applied spectral smoothing of ±10 Hz for frequencies >30 Hz and ±4 Hz for lower frequencies. These methods have now been successfully applied to neural data in a number of cases (7–10).

Eye Movements. Stimulus presentation and eye position monitoring were recorded and synchronized with neuronal data using the Experiment Control Module programmable device (FHC). Eye position was continuously monitored using an eye tracker system (EyeLink II; SR Research) with a binocular 1-kHz sampling rate. Eye position was calibrated before each experiment using a five-point calibration procedure in which the animal was required to fixate on each point (one in the center, two in the vertical, and two in the horizontal axes or the diagonals) in steps of 4°, 8°, and 12° from the central fixation spot. The eye-tracker gains were adjusted such as to be linear for the horizontal and vertical eye deflections. The fixation pattern was analyzed to rule out any systematic bias and inconsistency during fixation when identical stimuli were presented in different conditions (control and adaptation). Microsaccades were analyzed every 10 ms by using a vector velocity threshold of 10°/s (this corresponds to a 0.1° eye movement between consecutive 10-ms intervals). To rule out any systematic bias and inconsistency during the control and adaptation conditions, we analyzed the eye position on the x and y axes, as well as the number and speed of microsaccades (these measures did not depend significantly on stimulus condition). The changes induced by adaptation are uncontaminated by fixational eye movements: we found no statistically significant relationship between the horizontal/vertical saccade amplitude and frequency and stimulus condition (control vs. adaptation; $P > 0.2$, Wilcoxon signed-rank test for all comparisons).

1. Mitzdorf U (1985) Current source-density method and application in cat cerebral cortex: investigation of evoked potentials and EEG phenomena. *Physiol Rev* 65: 37–100.
2. Mitzdorf U, Singer W (1979) Excitatory synaptic ensemble properties in the visual cortex of the macaque monkey: A current source density analysis of electrically evoked potentials. *J Comp Neurol* 187:71–83.
3. Nicholson C, Freeman JA (1975) Theory of current source-density analysis and determination of conductivity tensor for anuran cerebellum. *J Neurophysiol* 38: 356–368.
4. Pettersen KH, Devor A, Ulbert I, Dale AM, Einevoll GT (2006) Current-source density estimation based on inversion of electrostatic forward solution: Effects of finite extent of neuronal activity and conductivity discontinuities. *J Neurosci Methods* 154: 116–133.
5. Green DM, Swets JA (1966) *Signal Detection and Psychophysics* (John Wiley & Sons, New York).
6. Macmillan NA, Creelman CD (2005) *Detection Theory: A User's Guide* (Lawrence Erlbaum Associates, Mahwah, NJ), 2 Ed.
7. Gregoriou GG, Gotts SJ, Zhou H, Desimone R (2009) High-frequency, long-range coupling between prefrontal and visual cortex during attention. *Science* 324:1207–1210.
8. Womelsdorf T, Fries P, Mitra PP, Desimone R (2006) Gamma-band synchronization in visual cortex predicts speed of change detection. *Nature* 439:733–736.
9. Mitra PP, Pesaran B (1999) Analysis of dynamic brain imaging data. *Biophys J* 76: 691–708.
10. Pesaran B, Pezaris JS, Sahani M, Mitra PP, Andersen RA (2002) Temporal structure in neuronal activity during working memory in macaque parietal cortex. *Nat Neurosci* 5: 805–811.

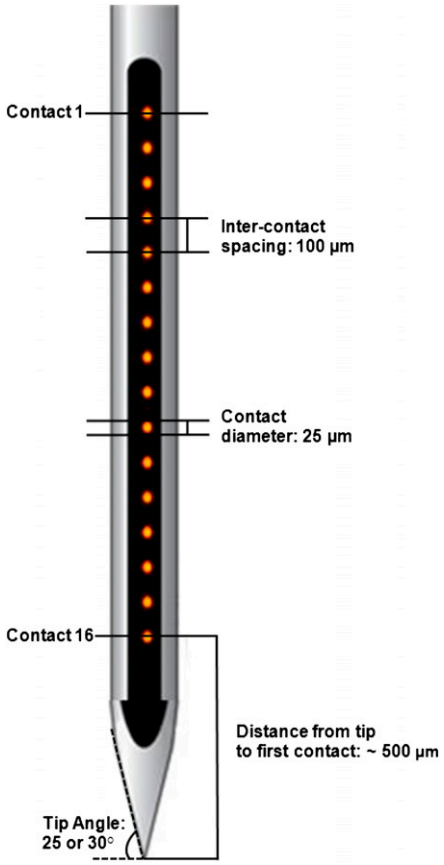

Fig. S1. Multicontact laminar electrode. Using multicontact laminar electrodes, we recorded simultaneously spiking activity from isolated individual neurons and LFP units across cortical layers of V1. Each probe consists of 16 equally spaced (100 μm) electrode contacts spanning a total length of 1.6 mm. Each electrode contact is 25 μm in diameter and is composed of platinum iridium. In half of the recording sessions, the laminar probe was treated with a carbon nanotube coating. The coating reduced the impedance by a factor of 25 without altering the area, resulting in an improvement in the signal-to-noise for both spikes (high-frequency band) and LFPs (low-frequency band).

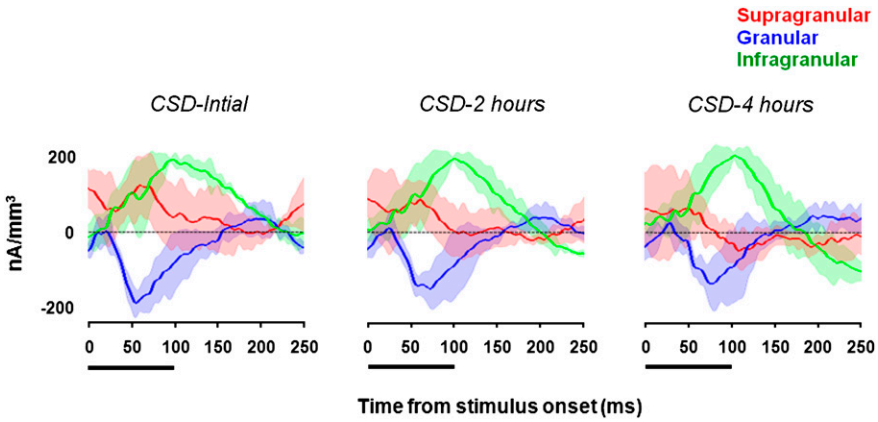

Fig. S2. Identification of cortical layers through current source density analysis. To identify cortical layers, we measured the ERP during a passive fixation task while monkeys were exposed to a full-field black screen that flashed white (≈1 Hz) for 100 ms and then returned to black. CSD (according to the second spatial derivate of the LFP time-series) was calculated to identify the polarity inversion accompanied by the sink-source configuration at the base of the granular layer. This analysis provides a more exact physiological assessment of the changes in neuronal excitability that forms the basis of the LFP signal. We assessed how stably the identification of cortical layers is maintained over time (left to right). In these examples, each plot represents the average CSD of those contacts assigned to a given layer. This allowed us to determine the precise timing of the initial sink (≈50–60 ms; the sink is inside layer 4; compare Fig. 1 *B* in main text) and compute the sink center of mass. CSD trace envelopes represent SD, and black bars indicate the duration of the flashed stimulus (100 ms).

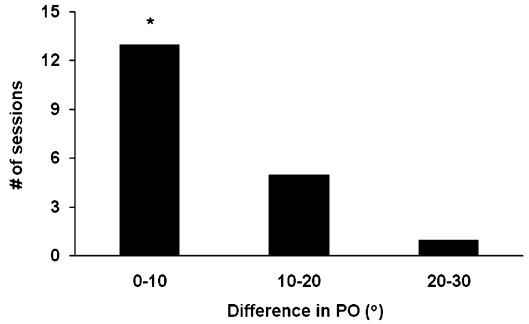

Fig. S3. Mean difference in preferred orientation across cortical layers for individual sessions. We first identified the tuning properties of local field potentials for each contact. For each recording session we averaged the differences in preferred orientation [determined using the vector averaging method (1–3)] between pairs of contacts. For more than 68.42% of sessions, the mean difference in orientation preference across pairs of contacts was within 10°. This indicates that the advancement of the laminar electrode remained isolated to a single cortical column in V1. *P = 0.0002, Wilcoxon signed-rank test.

1. Dragoi V, Sharma J, Miller EK, Sur M (2002) Dynamics of neuronal sensitivity in visual cortex and local feature discrimination. *Nat Neurosci* 5:883–891.
2. Dragoi V, Sharma J, Sur M (2000) Adaptation-induced plasticity of orientation tuning in adult visual cortex. *Neuron* 28:287–298.
3. Gutnisky DA, Dragoi V (2008) Adaptive coding of visual information in neural populations. *Nature* 452:220–224.

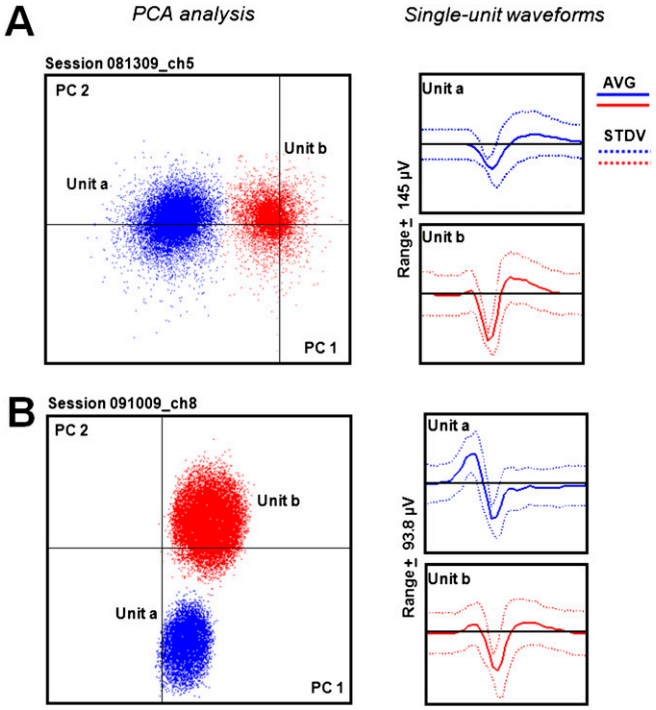

Fig. S4. Single unit isolation on the laminar electrode. (*A* and *B*) Two representative examples of electrode contacts in which individual neurons were isolated. Analysis consisted of using Plexon's Offline Sorter software package, which uses principal component analysis (PCA). Distinct clusters were identified based on spike waveform properties such as the weight of the first and second principal components (*Left*). In these examples, we have identified two units isolated on each channel and displayed their average waveform and SD (*Right*).

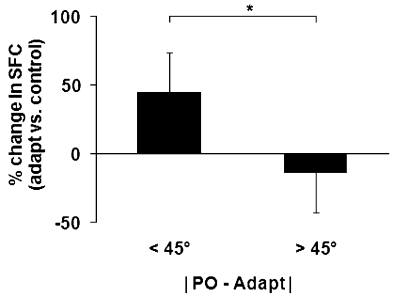

Fig. S5. Postadaptation change in gamma-band SFC is statistically significant only for test orientations within 45° of the adapting stimulus. SFC was calculated using the 300-μm pooling scheme (compare Fig. 4 *A* and *B*, main text). Changes in SFC after adaptation (calculated by averaging the SFC values across layers) were statistically significant only when the absolute difference between the preferred orientation (PO) of the cells and LFPs for a given penetration and the corresponding adapting stimulus ($\Delta\theta$) was <45° (*$P < 0.05$, Wilcoxon signed-rank test), consistent with previous studies (1, 2).

1. Dragoi V, Sharma J, Sur M (2000) Adaptation-induced plasticity of orientation tuning in adult visual cortex. *Neuron* 28:287–298.
2. Gutnisky DA, Dragoi V (2008) Adaptive coding of visual information in neural populations. *Nature* 452:220–224.

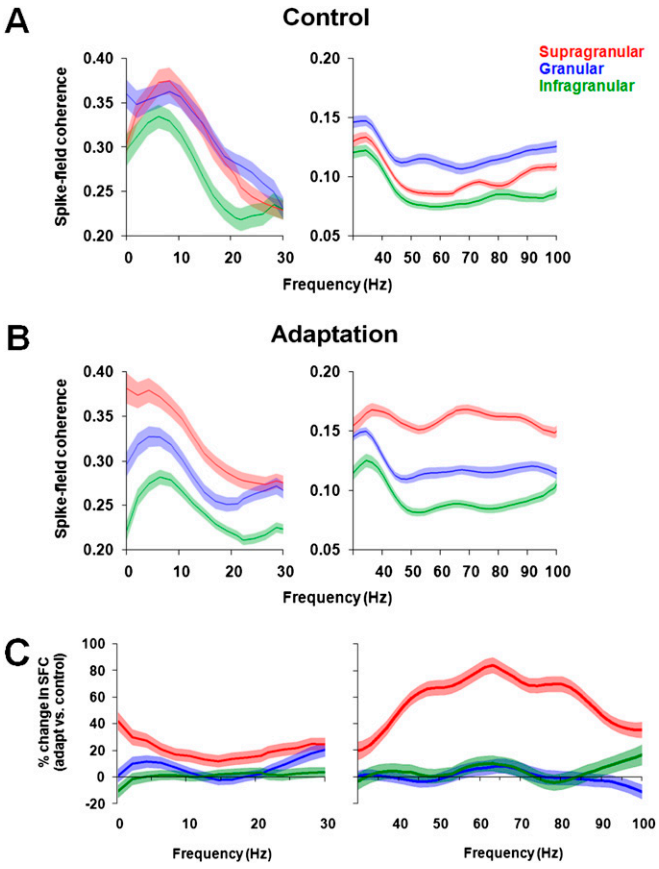

Fig. S6. Adaptation increases SFC for lower-frequency bands. (*A*) For the analysis of lower frequencies we used the multitaper method, in which we computed spike-triggered averages by averaging the LFP signal and applying ±4 Hz smoothing for frequencies <30 Hz (±10 Hz for frequencies >30 Hz). We observed no difference in SFC across cortical layers during the presentation of the control stimulus. (*B*) Adaptation increases SFC across all cortical layers between 0 and 30 Hz, with the largest increase occurring in supragranular and granular layers. (*C*) Percentage SFC change between adaptation and control was calculated separately for frequencies <30 Hz and for frequencies >30 Hz. For all traces in control and adaptation, shaded regions represent SEM.

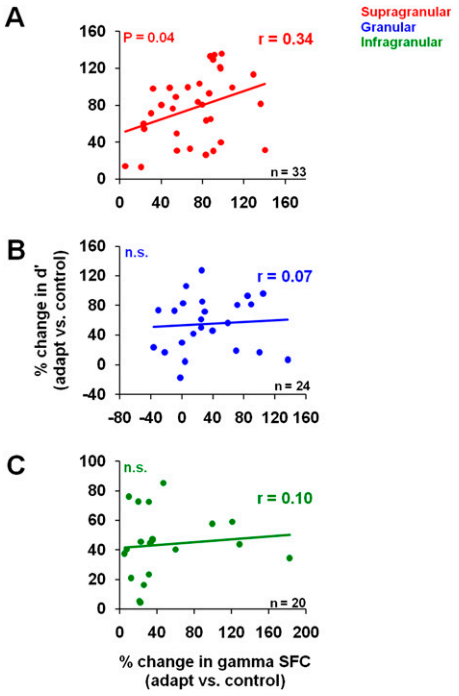

Fig. S7. "Within-layer" pooling scheme: the layer-specific relationship between the postadaptation changes in gamma synchronization and neuronal discrimination performance. (*A–C*) There is a significant positive correlation between the gamma-band SFC after adaptation and the change in *d′* that is specific to the supragranular layer ($r = 0.34$, $P = 0.04$, Pearson correlation). In contrast, granular and infragranular layer cells exhibited postadaptation changes in discriminability that were independent of the changes in SFC (granular: $r = 0.07$, $P = 0.73$; infragranular: $r = 0.10$, $P = 0.67$, Pearson correlation).

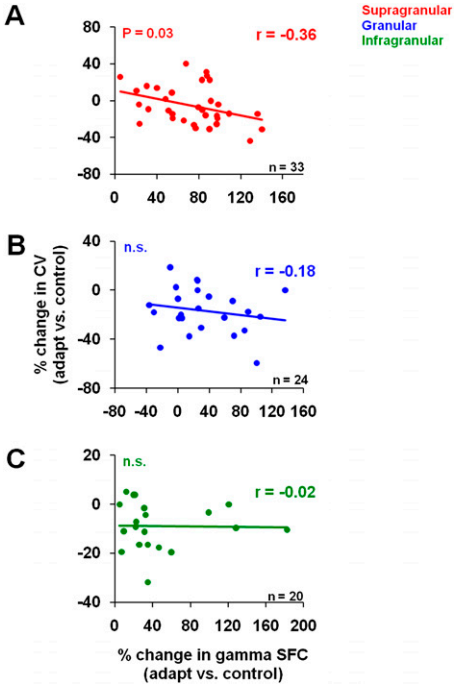

Fig. S8. Layer-specific relationship between gamma synchronization and neuronal precision. In addition to changes in discrimination performance after adaptation, we also measured neuronal precision by estimating the variation in the interspike interval as the coefficient of variation (1–3) (CV = SD/mean interspike interval). We found that only the recording sites in the supragranular layers were associated with a significant correlation between the postadaptation change in CV and the corresponding change in SFC (*A*; r = −0.36, $P = 0.03$, Pearson correlation). In contrast, neurons in granular and infragranular layers exhibited postadaptation changes in precision that were independent of the changes in SFC (*B* and *C*; granular: $r = -0.18$, $P = 0.38$; infragranular: $r = -0.02$, $P = 0.93$, Pearson correlation). Colored lines represent the linear regression fits associated with each cortical layer.

1. Mainen ZF, Sejnowski TJ (1995) Reliability of spike timing in neocortical neurons. *Science* 268:1503–1506.
2. Softky WR, Koch C (1993) The highly irregular firing of cortical cells is inconsistent with temporal integration of random EPSPs. *J Neurosci* 13:334–350.
3. Dayan P, Abbott LF (2001) *Theoretical Neuroscience* (MIT Press, Cambridge, MA).